Cylindrical and Spherical Active Coated Nanoparticles as Nanoantennas: Active nanoparticles as nanoantennas

Arslanagic, Samel; Ziolkowski, Richard W.

Published in:
I E E E Antennas and Propagation Magazine

Link to article, DOI:
10.1109/MAP.2017.2752648

Publication date:
2017

Document Version
Peer reviewed version

Cylindrical and Spherical Active Coated Nano-Particles as Nano-Antennas

Samel Arslanagić, *Member, IEEE*, Richard. W. Ziolkowski, *Fellow, IEEE*

***Abstract*—In this work we review the fundamental properties of several spherical and cylindrical, passive and active, coated nano-particles (CNPs) with emphasis on their potential for nano-antenna and nano-amplifier synthesis. For the spherical geometries, the nano-particles are excited by an electric Hertzian dipole, which represents, e.g., a stimulated atom or molecule. The cylindrical nano-particles are excited by a magnetic line source. In the active cases, gain is added to the core region of the particle. For simplicity, it is modelled by a canonical, frequency independent gain model. We demonstrate that specific CNPs can be designed to be resonant and well-matched to their respective excitation sources. With active cores, these designs can lead to extremely large total radiated powers. For both configurations, insights into the effects of the nano-particle material composition, source location and orientation will be given on the basis of studying their near-field and power flow density distributions, their total radiated powers, and their directivity properties.**

***Index Terms*— Dipole source, gain, line source, nano-amplifiers, nano-antennas, nano-particles, radiation, scattering**

I. Introduction

TRADITIONAL analyses of antennas originate from their radio frequency (RF) developments [1]. Transmitting antennas convert voltages and currents into electromagnetic waves, while receiving antennas convert electromagnetic waves into voltages and currents. Notable attention has recently been given to optical antennas, see [2-4] and the references therein. For instance, standard resonant antennas such as dipoles and bow-ties have been studied at visible wavelengths by many groups [5-9]. They are ones that are the most accessible to nano-fabrication processes; and, hence, their simulated properties have been experimentally verified. Dimers are another well-studied example of optical antennas specifically designed for enhancements of local fields [10-13]. More recent examples include Yagi-Uda antennas [14-16], arrays [17-20] and radiators combined with bandgap structures [21]. Even more traditional schemes, such as using an antenna to excite an RF waveguide, have been extended to optical frequencies [22]. Nonlinear loads have also been incorporated into optical nano-antennas to control their emission properties, as well as create harmonic generation [23-25].

S. Arslanagić is with the Department of Electrical Engineering, Technical University of Denmark, Bld. 348, Ørsteds Plads, 2800 Kgs. Lyngby, Denmark (e-mail: sar@@elektro.dtu.dk).

R. W. Ziolkowski is with the Department of Electrical and Computer Engineering, University of Arizona, Tucson, AZ 85721,USA, and the University of Technology Sydney, Global Big Data Technologies Centre, Ultimo NSW 2007, Australia (e-mail: ziolkowski@ece.arizona.edu).

Given the intrinsic nature of the excitation of the majority of optical antennas studied to date, most RF engineers would view them as nano-scatterers, which have been designed to create large local fields. Thus, in this respect, even a single properly designed nano-particle can be viewed as a nano-antenna. Consequently, most optical antennas have taken on the purpose of converting propagating electromagnetic waves to localized fields and vice versa [2]. To this end, we note that a variety of nano-particles of very different shapes have been considered as candidates for nano-antennas and related applications [2, 3, 26]. Nevertheless, whether one views its excitation as an incident electromagnetic wave or potentially a current driven source, an optical antenna is viewed as a transducer that acts to generate/receive an electromagnetic field. As a consequence, there have been studies [4] to apply classical impedance matching techniques to optical antennas, i.e., these scatterers have been modified to maximize the power radiated/accepted by the optical antenna.

In the past decade there has been considerable attention devoted to the field of metamaterials (MTMs), and significant advances have been accomplished encompassing applications from the microwave [27] to the optical [28] regimes. One area of emphasis has been the use of MTMs to engineer the performance characteristics of antennas [29]. One aspect of these studies has been to miniaturize antennas while maintaining their performance characteristics. In particular, MTM-inspired structures have been introduced to act as impedance transformers to realize matching of the overall antenna system to its source and to the wave impedance of the medium in which it is radiating. They offer some advantages over classical impedance matching methods for a variety of electrically small antenna systems. The idea to use a resonant MTM-inspired construct in the near field of an electrically small radiator to significantly enhance its performance characteristics was introduced in [30-32]. These theoretical models began with enclosing an infinitesimal radiating dipole (an electric Hertzian dipole) with a spherical double negative MTM shell [30]. It was then recognized [31, 32] that only a single negative (SNG) spherical MTM shell was required. For instance, the epsilon-negative (ENG) shell is an electrically small resonator, i.e., its core is an electrically small region excited by the electric field of the driven dipole and, hence, it acts as a capacitive element. Similarly, its shell is also excited by that electric field and has a capacitive response but is filled with a negative permittivity and, hence, acts as an inductive element. The combination of the lossy capacitive and

inductive elements yields a lossy (RLC) resonator. The driven element, the electrically small dipole antenna, has a large negative reactance, i.e., it too is a capacitive element. Because the lossy resonator is in the extreme near-field of the driven element, the fields involved and the subsequent responses are large. It was found that the reactance of this near-field resonant parasitic (NFRP) element, the ENG shell, can be conjugate matched to the dipole reactance by adjusting their sizes and material properties to achieve a resonance. By tuning the effective capacitances and inductances of both the driven and parasitic elements, the entire antenna can moreover be nearly completely matched to the source, i.e., the NFRP element also acts as an impedance transformer. By arranging the NFRP element so that the currents on it dominate the radiation process, a high radiation efficiency and, thus, a very high overall efficiency can be realized. Active MTM shells and active NFRP elements have been considered [33, 34] to overcome the physical limitations on the bandwidths of electrically small radiators [35, 36].

These concepts of tailoring electrically small, resonant, MTM-inspired constructs to enhance the performance of small driven antennas can be extended immediately to optical frequencies, i.e., to very electrically small radiators such as excited atoms or molecules. In particular, because nature gives us ENG materials, i.e., metals, in the optical regime, the optical geometry represented by a passive, spherical, metal coated nano-particle (CNP) excited by an electric Hertzian dipole (EHD) is a straightforward extension of the radio frequency case of an ENG shell near to or surrounding an electrically small dipole antenna considered in [37]. It was shown that specific core-shell particles can be resonant and thus lead to large enhancements of the total power radiated by the EHD in contrast to it radiating in free space alone. These core-shell geometries are representative of one of the very successful outcomes of MTM research, i.e., the realization that the juxtaposition of two materials, one with positive material parameters and the other with negative ones, can be used to create electrically small resonators [27]. As to the optical nano-antennas and CNP geometries reviewed above, the physics underlying this outcome is also tied with one of the best known effects associated with optics at surfaces, i.e., the occurrence of plasmons [38]. Despite the many advantages of plasmonic-based nano-antennas, their performance is, however, inevitably limited by the large losses associated with metals at optical frequencies. In order to alleviate the issue of losses, use of gain in plasmonic-based configurations has been proposed.

The introduction of gain into the negative-positive MTM-inspired subwavelength cavity design paradigm has led to the investigation of highly subwavelength planar [39] and spherical nano-laser [40], nano-sensing [41] and nano-amplifier [42] systems. This concept of juxtaposing metals and dielectrics in conjunction with gain media to form nano-laser resonators has led to truly impressive levels of miniaturization of lasers over the past few years (see, for example, the recent review [43]). These metallic/plasmonic nano-lasers have provided optical sources that are much smaller than a wavelength (see e.g., [44-50]). Gain has also been introduced to overcome the losses associated with metal-based optical MTMs [51-59] and with plasmonic systems [60-65]. Experimental verification of a version of the highly subwavelength nano-particle lasers has been reported with an optically pumped, dye-impregnated coating [66]. Experimental demonstration of complete compensation of losses in metallic-based optical MTMs was reported in [67] using a fishnet MTM having an optically pumped dye-impregnated core. Moreover, based on the seminal work [68] that plasmon-based amplification is possible, even smaller plasmon-based systems have been investigated, including potential localized photonic sources, sensors and amplifiers (see, e.g., [69-71]). The first experimental observation of the lasing spaser [70] was achieved in [72] with using optically pumped PbS semiconductor quantum dots.

We note that, apart from the loss compensation achieved in plasmonic-based systems impregnated with gain, recent years have witnessed the emergence of an alternative and very interesting route towards low-loss nano-photonic structures. To this end, a very successful exploitation of resonant high-index dielectric (and even semiconductor) material building blocks has been demonstrated for a variety of nano-antennas, optical MTMs and metasurfaces, see e.g., [73]-[76] and the list of references therein.

In this manuscript we review our work on active nano-antennas and nano-amplifiers formed by specifically designed CNPs. In light of our introductory survey above, the examined CNPs in the presence of relevant excitation sources do indeed make a nano-antenna system. Therefore, we will use the designation CNP or nano-antenna interchangeably. As reported in [3, Ch. 3], [42, 77, 78], both enhanced and reduced radiation/scattering effects can be achieved in various CNP configurations. In particular, specific spherical CNPs, denoted here as S-CNPs, can be designed to be resonant and well-matched to the radiating EHD, which leads to large enhancements in the total radiated power. Treating a stimulated atom or molecule as an idealized EHD, the enhanced total radiated power of such a nano-antenna, for instance, would have a significant impact on its application as a nano-sensor for fluorescence analyses [78]. On the other hand, other nano-antenna designs can significantly reduce emissions. It has been shown that CNP designs can effectively jam the fields radiated from a single or from multiple emitters [42, 77, 78]. Non-radiating or dark states associated with the passive configurations were recognized in [79]. These non-radiating states can be connected directly to the transparency /cloaking effects introduced by Alù and Engheta (see, for instance, [80] and the references therein). Not only S-CNPs have been studied, but the radiation characteristics of passive [81] and active [3, Ch. 3], [82, 83] circular cylindrical CNPs, denoted here as CC-CNPs, have also been studied under plane wave and magnetic line source excitations. In contrast to the S-CNPs whose response is polarization independent, the CC-CNPs' performance characteristics are polarization dependent, as one would expect from any elongated geometry. Moreover, the impact of the composition and the sizes of the CNPs [3,

Ch. 3], [77] and directivity effects of both S-CNPs and CC-CNPs [84] have also been investigated.

In this work, we only address the resonant CNPs with enhanced total radiated power responses. Both S-CNP and CC-CNP configurations will be treated. Insights into the effects of the orientation of the exciting dipole on the field enhancement will be given; and, moreover, the influence of the locations of the respective excitation sources on the resonant properties of the S- and CC-CNPs will be addressed. Examples of the directivity effects and the local near-field and power flow distributions will be illustrated.

The manuscript is organized in the following manner. Section II introduces the S- and CC-CNP configurations, and outlines briefly the details of the analytical solution. In Section III the material composition of the CNPs, as well as the gain model for the active cases, are discussed. Section IV summarizes the numerical results pertaining to both the S-CNPs and the CC-CNPs. Finally, Section V summarizes and concludes the work. Throughout the manuscript, the time-factor,$\exp(j\omega t)$, with ω being the angular frequency, and t being the time, is assumed and suppressed.

II. Configurations and Analysis Methods

A. Configurations

The spherical coated nano-particle (S-CNP) and circularly cylindrical coated nano-particle (CC-CNP) configurations reviewed in here are shown in Figure 1. The abbreviation CNP will be used throughout when reference is made to the properties and results common to both geometries. Otherwise, the S-CNP and CC-CNP abbreviations will be used to specifically refer to the spherical and cylindrical geometries, respectively.

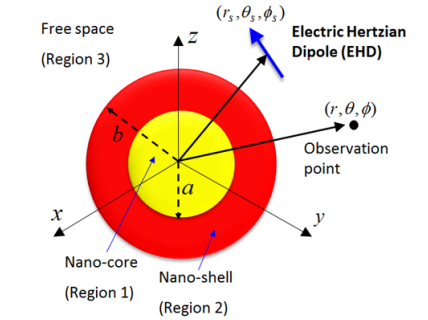

(a) S-CNP

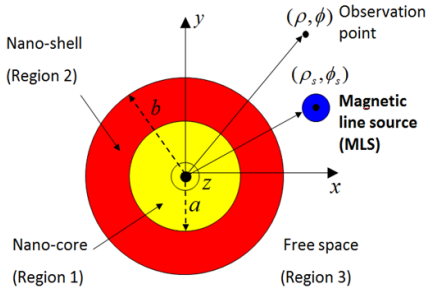

(b) CC-CNP

Fig. 1. The examined S-CNP and CC-CNP configurations.

In both cases, the CNPs consist of a nano-core (region 1) of radius a covered concentrically by a nano-shell (region 2) with an outer radius b. The CNP is immersed in free-space (region 3) characterized by the permittivity, ε_0, and the permeability, μ_0. Thus, in region 3 the intrinsic impedance, $\eta_0 = \sqrt{\mu_0/\varepsilon_0}$, and the wave number, $k_0 = \omega\sqrt{\varepsilon_0\mu_0} = 2\pi/\lambda_0$, where λ_0 denotes the free-space wavelength. Regions 1 and 2 consist of simple (isotropic, linear, and homogeneous) and, in general, lossy materials with permittivities, permeabilities, and wave numbers given by $\varepsilon_i = \varepsilon_i' - j\varepsilon_i''$, $\mu_i = \mu_i' - j\mu_i''$, and $k_i = \omega\sqrt{\varepsilon_i\mu_i}$, respectively, with $i = 1$ for region 1, and $i = 2$ for region 2. The specific choices of the materials employed in this review will be detailed in Section III.

The S-CNP is illuminated by the incident field generated by an arbitrarily located and oriented electric Hertzian dipole (EHD) with the dipole moment $\boldsymbol{p} = \boldsymbol{a}_p p$; the unit vector $\boldsymbol{a}_p$ is its orientation, while p [Am] is its complex amplitude which typically is expressed as the product of the constant electric current I_e [A] driving the EHD and its length l [m], i.e., $p = I_\mathrm{e} l$. A spherical coordinate system (r,θ,ϕ), and the associated rectangular coordinate system (x,y,z), are introduced such that the origin of these coincides with the centre of the S-CNP. The coordinates of the observation point are (r,θ,ϕ), while those of the EHD are (r_s,θ_s,ϕ_s).

The CC-CNP is illuminated by the incident field generated by an arbitrarily located infinitely long magnetic line source (MLS) which is driven by a constant magnetic current I_m [V]. This corresponds to the transverse electric (TE) polarization. The MLS, as opposed to an electric line source, is required in here in order to excite resonances in the CC-CNPs of interest to this work [81, 82]. A circular cylindrical coordinate system (ρ,ϕ,z), and the associated rectangular coordinate system (x,y,z), are introduced such that the origin of these coincides with the cross-sectional centre of the CC-CNP, and such that the entire configuration is infinite along the z-direction, with the MLS being parallel to the axis of the cylinders. The coordinates of the observation point are (ρ,ϕ), while those of the MLS are (ρ_s,ϕ_s).

B. Analysis Methods

Detailed analytical solutions of the canonical CNP configurations have been derived previously for spherical [37, 42, 84] and circular cylindrical geometries [81, 82, 84]. Here we summarize the main steps of the solution procedure and include the most important results needed to characterize the performance of the examined configurations.

The solution procedure for the S-CNP configuration problems is as follows. The field due to the EHD, which constitutes the known incident field, is represented as a multipole expansion of transverse magnetic (TM) and transverse electric (TE) spherical waves. The unknown scattered fields in the three regions are likewise expanded in terms of TM and TE spherical waves. Their unknown expansion coefficients depend on the EHD location, the orientation of the EHD, and the composition of the S-CNP. They are obtained by enforcing the boundary conditions on the

two spherical interfaces, $r = a$ and $r = b$. With the expansion coefficients known, the fields at all points inside and outside the S-CNP are known. Beside the near-field field distributions, we devote attention in our investigations to the so-called normalized radiation resistance (NRR), the directivity, and the distributions of the power flow density. The NRR is defined as the radiation resistance $R_{S,t}$ of the EHD radiating in the presence of the S-CNP, normalized with the radiation resistance R_{EHD} of the EHD radiating alone. Thus,

$$\text{NRR} = 10 \cdot \log_{10} \frac{R_{S,t}}{R_{EHD}} = 10 \cdot \log_{10} \frac{P_{S,t}}{P_{EHD}}, \qquad (1)$$

where $P_{S,t} = R_{S,t} |I_e|^2/2$ is the total power radiated by the EHD in the presence of the S-CNP, and $P_{EHD} = R_{EHD} |I_e|^2/2$ is the total power radiated by the EHD alone. The explicit expressions of the radiated powers can be found in [37]. The directive properties of the S-CNPs are examined through the directivity which expresses the radiation intensity in a given direction normalized with the average radiation intensity; see e.g., [84] for its analytical expression. The power flow density distribution is examined though the Poynting vector, $\boldsymbol{S}(r, \theta, \phi)$, (its magnitude S and direction $\boldsymbol{a}_S$) given by $\boldsymbol{S} = \boldsymbol{a}_S S = 0.5\,\text{Re}\{\boldsymbol{E} \times \boldsymbol{H}^*\}$, with $\boldsymbol{E}$ and $\boldsymbol{H}$ being the total electric and magnetic fields, respectively.

The CC-CNP solution is obtained in a similar way. The MLS field, which is the known incident field, is expanded in terms of cylindrical wave functions. This is also the case with the unknown scattered fields in the three regions. The scattered field expressions contain the unknown expansion coefficients which depend on the location of the MLS and are obtained by enforcing the boundary conditions at the two cylindrical interfaces, $\rho = a$ and $\rho = b$. Once the expansion coefficients are known, the fields at all points interior and exterior to the CC-CNP are known, and several derived quantities can be introduced to characterize the performance of the CC-CNPs. Specifically, the NRR for the CC-CNP is defined as the radiation resistance $R_{C,t}$ of the MLS radiating in the presence of the CC-CNP, normalized with the radiation resistance R_{MLS} of the isolated MLS in free space. Thus,

$$\text{NRR} = 10 \cdot \log_{10} \frac{R_{C,t}}{R_{MLS}} = 10 \cdot \log_{10} \frac{P_{C,t}}{P_{MLS}}, \qquad (2)$$

where $P_{C,t} = R_{C,t} |I_m|^2/2$ is the total power radiated by the MLS in the presence of the CC-CNP, while $P_{MLS} = R_{MLS} |I_m|^2/2$ is the total power radiated by the MLS alone; their explicit expressions can be found in [81]. The directivity of the CC-CNP configuration takes on the form given in [84], while the power flow density is accounted for through the Poynting vector $\boldsymbol{S}(\rho, \phi)$ defined in a similar manner as for the S-CNP.

From (1) and (2), we note that the NRR is equivalent to the radiated power ratio introduced in the initial MTM-based antenna studies [30, 31]. Moreover, the NRR is equivalent to the Purcell factor (effect) [85, 86] which is associated with the enhancement of a molecule's spontaneous emission by its surroundings.

III. Gain and Material Models

The geometric and material parameters, as well as the gain model used in our CNPs are summarized next. For all CNPs, their nano-core is made of the dielectric silica (SiO_2), for which $\varepsilon_1 = 2.05\varepsilon_0$, $\mu_1 = \mu_0$, and $k_1 = k_0 n$, with $n = \sqrt{2.05}$ being its refractive index at the wavelengths of interest. Their nano-shells are made of either the metal (plasmonic material at the frequencies of interest) silver (Ag), gold (Au) or copper (Cu); the corresponding CNPs will be referred to as the Ag-, Au-, and Cu-based CNPs. In all cases, and unless indicated otherwise, the radius of the nano-core is set to $a = 24$ nm, while the radius of the CNP, the outer radius of the shell, is set to $b = 30$ nm. Since the plasmonic nano-shell is only 6 nm thick, accurate modelling of its optical properties requires taking into account the size-dependent behaviour of its permittivity ε_2 (note that the employed plasmonic materials are all non-magnetic, i.e., $\mu_2 = \mu_0$). These plasmonic nano-shells exhibit rather significant intrinsic size dependencies, which arise when the material size is comparable to and/or less than the bulk mean free path length of the conduction electrons in the material (see, e.g., [28, 40, 41] and the references therein). These size-dependencies are incorporated into the Drude model describing the metals in terms of a size dependent damping frequency term. As described in [40], empirically determined bulk values for the permittivity of the employed plasmonic materials are available in the wavelength range from 200 to 1800 nm; these were successfully used in [40]-[42]. The focus here is on the CNPs performance in the visible range from 450 to 700 nm. For the three plasmonic materials of present interest, Figure 2(a) shows the real part of the permittivity, ε_2', normalized with the free-space permittivity, ε_0, while Figure 2(b) shows the associated loss tangents, defined by $\text{LT} = \varepsilon_2''/|\varepsilon_2'|$. It is found that the real part of the permittivity of the three plasmonic materials is negative in the shown wavelength range. Furthermore, they all exhibit notable losses with Ag being the least lossy case. We note that in contrast to the plasmonic nano-shells, there are no size-dependent effects inside the dielectric silica nano-core.

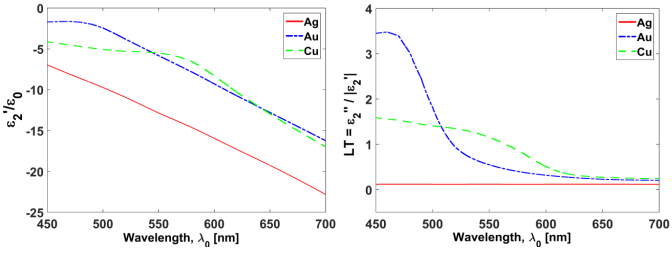

(a) (b)

Fig. 2. (a) The real part, ε_2', of the permittivity of the 6 nm thick Au, Ag, and Cu nano-shells normalized to the free-space permittivity ε_0, and (b) the corresponding loss tangents $\text{LT} = \varepsilon_2''/|\varepsilon_2'|$.

The plasmonic losses shown in Figure 2 are expected to deteriorate the performance of the associated CNPs. To achieve enhanced characteristics, they must be overcome by, e.g., including a gain material inside the CNPs. In this work, we make use of a canonical, frequency independent gain

model which will be introduced into the silica nano-core. According to such a model, the permittivity of the silica nano-core reads $\varepsilon_1 = \varepsilon_0(n^2 - \kappa^2 - 2jn\kappa)$ where n is the refractive index which is maintained at the value for the lossless silica nano-core, i.e., $n = \sqrt{2.05}$. Moreover, the parameter κ determines the nature of the nano-core and thus of the CNP. For $\kappa = 0$ and $\kappa > 0$, one has a *passive* nano-core, and thus a passive CNP. On the other hand, $\kappa < 0$ models an *active* nano-core, and thus an active CNP. Thus, the parameter κ represents the loss/gain constant [40].

The choice to use a constant gain parameter simplifies tuning the model to achieve its maximum performance. It is, however, important to note that realistic gain materials are dispersive. Therefore, in practice, one would chose the gain material, e.g., a quantum dot medium [87], such that ideally the resonance frequency at which its gain is maximized overlaps with the resonance frequency of the CNPs being designed or as much of its gain bandwidth as possible does. This will, of course, impose several challenges to be overcome towards the final optimized design since the presence of realistic media inevitably affects the very sensitive locations and response amplitudes of the CNP resonances.

IV. Numerical Results

Both the near and far field behaviours of a variety of passive and active CNPs shown in Figure 1 have been studied in our previous works [3, Ch. 4], [37, 42, 77, 78, 81, 82, 84]. The results for the passive cases indicate where the geometry resonances occur, which can be tuned by the geometry shape/size and the material parameters. The active cases must be retuned slightly with the presence of the gain material. They illustrate how gain help overcome the losses to achieve significant enhancements of the total radiated power. Below we highlight the main results that have been obtained for both the spherical and cylindrical CNPs.

We emphasize that all of our structures reviewed below have been designed to support a strong resonant dipole mode of operation. To this end, it is important to note that numerous related studies of the resonant dipole and higher order mode effects have been reported in passive plasmonic-based spherical [2, 3, 86, 88, 89, 90] and infinitely long cylindrical [91, 92] nano-particles. The attention was devoted to not only the standard canonical shapes, but also to particles of distinctively different shapes [26]. Moreover, a geometry similar to our S-CNP, consisting of metamaterials or passive plasmonic materials, was examined in [93] for higher order mode excitation and directive nano-antenna synthesis. Apart from the passive cases, active spherical nano-particles were considered as nano-lasers, spasers and super-scatterers supporting a resonant dipole mode [40, 66, 69, 71]. Drastically enhanced scattering properties, similar to the ones reviewed below, were also reported for active truncated cylindrical CNPs [3, Ch. 4], [83], as well as core-shell cubic box- [94] and rod-like [95] nano-particles. Furthermore, as a very flexible and low-loss route towards efficient resonant nano-antennas, all-dielectric high-index nano-particles supporting a multitude of modes has received much attention in recent years, see e.g., [73] and the works referenced therein.

A. Spherical CNPs

The NRR behaviours reported below and the near-field characteristics of the S-CNPs excited with a single or with multiple EHDs were reported in [3, Ch. 4], [42, 77, 78]. Their directivity behaviours were studied thoroughly in [84]. In this work, only the results pertaining to a single EHD excitation, as illustrated in Figure 1(a), are reviewed for both x- and z-oriented EHD excitations. Note that they correspond to EHD orientations which are normal and tangential to the spherical surfaces of the S-CNP. For both cases, its dipole moment is set to 5 A-nm, and unless otherwise stated, the EHD is located along the positive x-axis, at a distance of $r_s = 12$ nm.

A.1 NRR and near-field distributions

In Figure 3 we show the NRR as a function of the wavelength, λ_0, for the Ag-based S-CNP. The results in Figure 3(a) hold for a passive S-CNP for which $\kappa = 0$, while the results in Figure 3(b) hold for the so-called super-resonant, active Ag-based S-CNP.

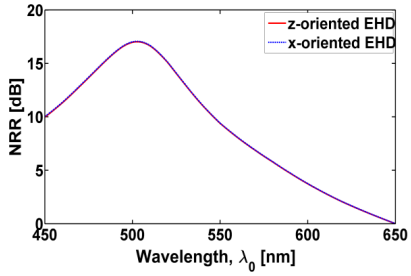

(a)

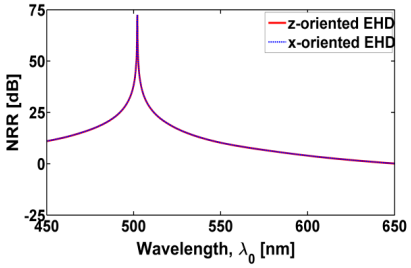

(b)

Fig. 3. The NRR as a function of the wavelength, λ_0, for a passive Ag-based S-CNP (a) and a super-resonant, active Ag-based S-CNP (b). In all cases, the EHD is located in the silica nano-core at $r_s = 12$ nm. The results for both the x- and z-oriented EHD excitations of the S-CNP are given.

The super-resonance behaviour is attained for $\kappa = -0.245$. In both cases, the results are shown for the two orthogonal EHD orientations when the EHD is located in region 1 at $r_s = 12$ nm. Figure 3 tells us that for a given value of κ, identical values of the NRR are obtained in the depicted wavelength range for the two EHD orientations. This is an expected consequence of the spherical nature of the examined CNP. The value of $\kappa = -0.245$ was found to lead to the largest NRR value for both EHD orientations, around 72.5 dB at 502.1 nm in Figure 3(b). This corresponds to a super-resonant state for which the NRR is significantly increased

and the intrinsic plasmonic losses in the nano-shell part of the S-CNP have been vastly overcome. This configuration is referred to as a super-resonant S-CNP. These super-resonant S-CNP results are significantly different in comparison to the corresponding passive Ag-based S-CNP values. In the latter, the largest NRR value is found to be several orders of magnitude lower than the corresponding super-resonant S-CNP value, i.e., the peak NRR value in Figure 3(a) is 17 dB at 502.7 nm, around 55.5 dB lower than its value in Figure 3(b). Therefore, as also found in the case of a plane wave excited S-CNP [40] and other active nano-particles [94, 95], the inclusion of gain provides a means to overcome the losses present in the S-CNP, and leads to a major enhancement of the total radiated power.

Although not reviewed here, similar super-resonance outcomes can be obtained with the Au- and Cu-based S-CNPs [3, Ch. 4]. The values of the NRR, the parameter κ and the wavelength λ_0 for the corresponding super-resonant Ag-, Au-, and Cu-based S-CNPs are summarized in Table 1. It is found, as expected, that the magnitude of κ needed to excite a super resonance response in the investigated S-CNPs is largest for the Cu-based S-CNP since this is the lossiest of the three cases, cf., Figure 2. The gain needed for the super-resonance in the Ag-based S-CNP is almost the same as for the super-resonant active rod-like CNPs of identical material composition and comparable cross-sectional sizes [3, Ch. 3], [83]. Moreover, the gain value reported in Table 1 for the Au-based S-CNP is higher than for the active gold-shell cubic box- [94] and the gold-core rod-like [95] particles of comparable cross-sectional sizes.

Parameter	Ag	Au	Cu
NRR [dB]	72.5	74.0	68.5
κ	-0.245	-0.532	-0.741
λ_0 [nm]	502.1	597.4	601.7

Tab. 1. Summary of various parameters for the super-resonant Ag-, Au-, and Cu-based S-CNPs when the EHD is inside the nano-core at $r_s = 12$ nm. The results hold irrespective of the EHD orientation.

In order to explain the super-resonances in Figure 3(b), and thus to shed further light on the properties of the Ag-based S-CNPs, investigations into the behaviour of the near fields were conducted. To this end, the quantity $10 \cdot \log_{10}|E_\theta|$, where the θ-component of the total electric field, E_θ, is normalized by 1 V/m, was selected to graphically investigate these fields. The plane of observation is taken to be the xz-plane, and the distributions of this electric field quantity are depicted in a circular region with a radius of 90 nm. In Figures 4(a) and 4(b) we show the super-resonant Ag-based S-CNP results for both the z- and x-oriented EHDs, respectively, when $\kappa = -0.245$ and $\lambda_0 = 502.1$nm. Recall that these parameter values produce the peaks in the NRR values reported in Figure 3(b). For comparison, Figures 4(c) and 4(d) show the electric field of the corresponding passive Ag-based S-CNP configurations for $\kappa = 0$ and $\lambda_0 = 502.7$nm. In all cases, the curves representing the spherical surfaces of the S-CNP are also shown. As expected, the modes excited in the Ag-based S-CNP, as shown in Figures 4(a) and 4(b), are clearly dipolar.

In Figure 4(a), the distribution corresponds to a z-oriented dipole, while to a x-oriented dipole in Figure 4(b), located at the origin. Moreover, these two orthogonal dipole modes are found to be very strongly excited and are of comparable magnitude. This rather strong excitation of the dipole mode inside the S-CNP is the cause of the observed super resonance effects illustrated in Figure 3(b). This result firmly demonstrates that the inclusion of gain helps overcome the intrinsic plasmonic losses in the S-CNP. In contrast, since the S-CNP is passive, the field distributions for the two EHD orientations in Figures 4(c) and 4(d) are only weakly dipolar. These relatively low field levels correspond to the much lower values of the NRR in Figure 3(a). Similarly, we note that the near-field results found for the Au- and Cu-based S-CNPs yield the same conclusions, and are therefore not included here.

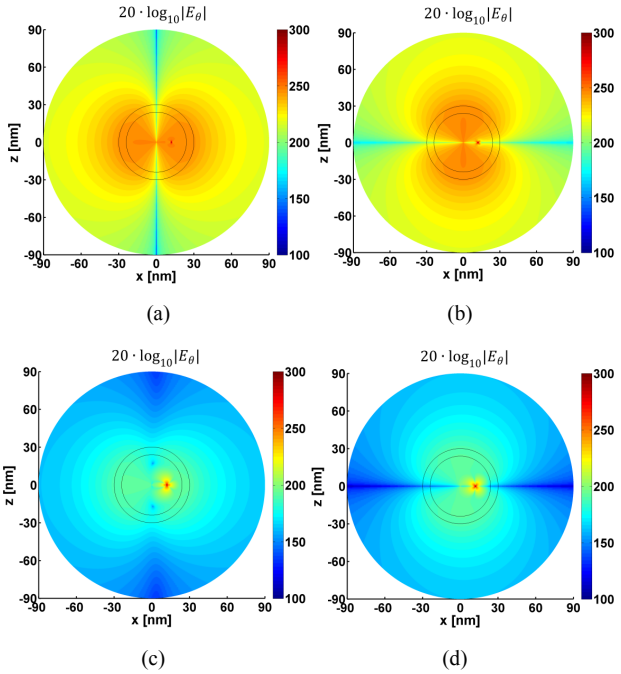

Fig. 4. The magnitude of the θ-component of the electric field of the super-resonant Ag-based S-CNP for the (a) z-oriented EHD and the (b) x-oriented EHD. The results for the corresponding passive Ag-based S-CNPs are found in (c) and (d). In all cases, the EHD is located along the x-axis inside the nano-core at $r_s = 12$nm. The spherical surfaces of the S-CNP are also shown.

From the previous studies on related metamaterial-based spherical scatterers [37], [96], it is known that a resonance will occur for electrically small structures shown in Figure 1(a) when the approximate condition

$$\frac{a}{b} \approx \sqrt[2n+1]{\frac{[(n+1)\varepsilon_0 + n\varepsilon_2'][(n+1)\varepsilon_2' + n\varepsilon_1']}{n(n+1)(\varepsilon_2' - \varepsilon_0)(\varepsilon_2' - \varepsilon_1')}} \tag{3}$$

is satisfied. Specifically, the condition in (3) ensures very large amplitudes of the TM coefficient for the scattered field in the region outside of the S-CNP. This leads to the observed large NRR values. As discussed in [37, 96] for lossless and low-loss configurations, at least one of the parameters, ε_1' or

ε_2', must be negative in order for (3) to be satisfied. For the investigated Ag-based S-CNP we have that $\varepsilon_1' = 1.99\,\varepsilon_0$, and $\varepsilon_2' = -9.85\,\varepsilon_0$ at the super-resonant wavelength, 502.1 nm. Inserting these values in (3), with $a = 24$ nm and $n = 1$ (since the super-resonance is due to the dipole mode), one obtains $b \approx 29.5$ nm, which is close to the exact value of 30 nm. Of course, the condition (3) is also satisfied for the Au-, and Cu-based S-CNPs. Thus, (3) is quite useful to provide an initial guess of the resonant structure parameters for extensive numerical optimizations to determine the more exact values. The resonant phenomenon in the field expansion coefficients for spherical particles has recently been described in a very detailed manner in [97].

Although not shown here, we note that the super-resonant effects in the S-CNPs were examined as a function of their size. As expected, the optimal gain constant increases in value as the active CNP becomes smaller, i.e., more gain is needed to achieve the super-resonant state for electrically smaller configurations which maintain the ratio (3) because the losses increase for the correspondingly thinner metallic shells and less gain material is present due to their smaller cores.

A.2 Effects of EHD locations

The existence of the super-resonances in the active S-CNPs is not restricted to EHD locations inside their nano-cores. Figure 5 shows the NRR values as a function of the EHD distance r_s from the centre of the super-resonant Ag-based S-CNP to its exterior for the z-oriented EHD excitation, Figure 5(a), and for the x-oriented EHD excitation, Figure 5(b). These results demonstrate that the large NRR enhancements also occur when the EHD is located anywhere in the nano-cores and only begin to reduce in magnitude once it is located in the exterior to the S-CNP and is not as strongly coupled to it. The corresponding Au- and Cu-based S-CNPs clearly exhibit the same behaviour.

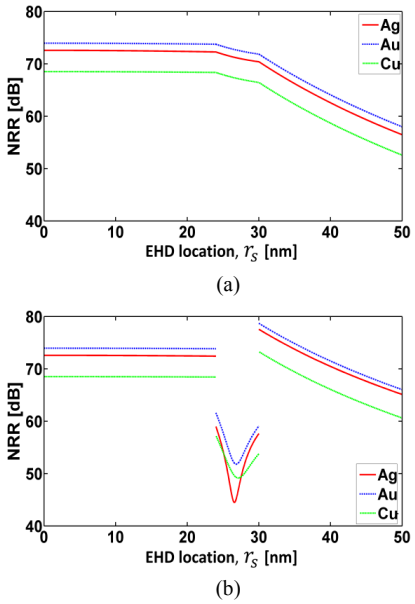

Fig. 5. The NRR as a function of the EHD location, $r_s \in [0,50]$ nm, for the super-resonant Ag-, Au-and Cu-based S-CNPs for the (a) z-oriented and (b) x-oriented EHD excitation.

While the NRR for the two EHD orientations both qualitatively and quantitatively resemble one another for EHD locations inside the nano-core, where an almost constant NRR is observed, this is not the case for locations outside of it. In particular, two notable differences are observed. First, the NRR of the x-oriented EHD drops significantly when the EHD enters the region of the nano-shells. Clear minima are found. In contrast, the NRR decreases moderately and slowly as the EHD moves through the nano-shells for the z-oriented EHD. At these locations, the excitation of the resonant dipole mode is obviously not nearly as pronounced for the x-oriented EHD as when the EHD is located inside the nano-core. Due to the x-orientation of the EHD, some of its field gets trapped inside the nano-shell (i.e., because the EHD is oriented orthogonal to its walls, the nano-shell acts as a waveguide excited by it), and thus does not get radiated. This results in the reported reduced NRR values.

The second notable difference between the two EHD orientations occurs when the EHD is moved into the exterior of the CNPs. In this case, the NRR values for the z-oriented EHD are below those obtained when it is in the interior. This behaviour is due to the decreased coupling between the EHD and the S-CNP. In contrast one finds that the largest NRR values for the x-oriented EHD occur when it is moved just outside the S-CNP. For these initial outside locations, the NRR values surpass those of the z-oriented EHD, irrespective of the location of the latter. This is next confirmed by the power flow density (or, more precisely, by the quantity $10 \cdot \log_{10}|\boldsymbol{S}|$, with $\boldsymbol{S}$ being the Poynting vector defined in Section II.B and normalized by 1.0 $\mathrm{W/m^2}$) shown for the S-CNP in Figure 6(a), for the z-oriented EHD, and in Figure 6(b), for the x-oriented EHD; in both cases, the EHD is located outside the CNP at $r_s = 32$ nm along the positive x-axis. The colours represent the magnitude of the Poynting vector, while the arrows show its directions.

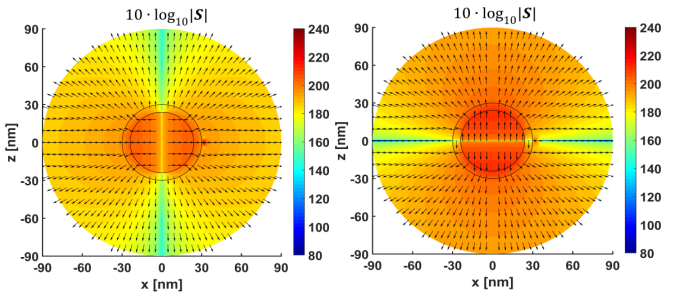

Fig. 6. Magnitude (color) and direction (arrows) of the power flow for Ag-based S-CNP for the (a) z-oriented EHD and (b) x-oriented EHD. In both cases, the EHDs are located outside the S-CNP, along the positive x-axis at $r_s = 32$ nm. The spherical surfaces of the S-CNP are also shown.

Clearly, the response for the x-oriented EHD is characterized by a stronger amplitude of the dipolar power flow, this being in line with the NRR results reported in Figure 5 for the two orientations of the EHD. We note that x-oriented EHD not only excites the resonant mode of the electrically small core-shell cavity, it also directly drives surface plasmon polaritons (SPPs) on the outer shell. Because

the shell is thin, these surface waves extend into the core and in turn are amplified by the presence of the gain medium. Because of their decaying amplitude behaviour away from the interface, the amplification is not large because the resulting coupling to the core is weak. Thus, while the strongest excitation of the resonant dipole mode, and thus the largest attainable NRR, requires the z-oriented EHD to be inside the nano-core, the locations of the strongest excitations are those just outside of the S-CNP for an x-oriented EHD.

The relative insensitivity of the very large NRR values to the EHD location in the interior and the immediate exterior of the active S-CNP suggests that it would be a very good candidate for a highly localized nano-sensor. Simply having it tuned to a dipole source near to it, such as a fluorescing molecule, the power reaching the far field is significantly amplified. Moreover, the large field localization near to the S-CNP indicates that its performance as a near-field resonant parasitic (NFRP) nano-antenna is also very good.

A.3 Directivity

The results in Figure 5 revealed interesting differences between the super-resonant Ag-based S-CNP for the z- and x-oriented EHDs. Figure 7 shows the corresponding directivity of the Ag-based S-CNP for varying values of the parameter κ for the z-oriented EHD case at the wavelength $\lambda_0 = 502.1$ nm. The E-plane (xz-plane) results are shown in Figure 7(a) and the H-plane (xy-plane) results are shown in Figure 7(b).

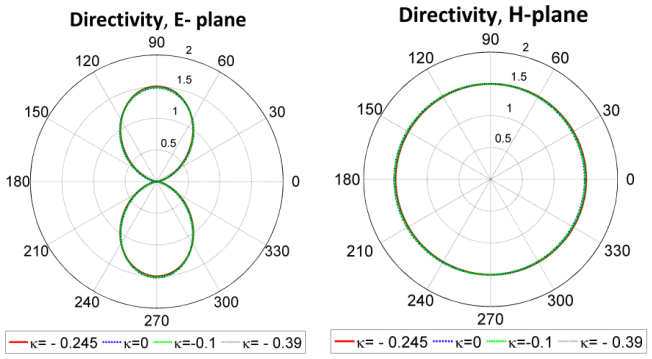

(a) (b)

Fig. 7. The directivity for the spherical Ag-based S-CNP for a z-oriented EHD located along the x-axis at $r_s = 12$ nm for different values of the parameter κ. The E-plane (xz-plane) pattern is shown in (a), and the H-plane (xy-plane) pattern is shown in (b).

Despite the large NRR shown in Figure 3(b) and Figure 5, the directivity of the super-resonant state, which is clearly dipolar, is not enhanced relative to that of an isolated z-oriented EHD, i.e., the directivity is independent of κ. In fact, it is the same as that of the passive S-CNP ($\kappa = 0$). Because of the electrically small size of the S-CNP, it simply radiates as an electrically small dipole (with an azimuthally symmetric pattern in the H-plane) with a maximum directivity around 1.5. Although not shown, the same overall conclusions apply to the directivity for the x-oriented EHD case. Except for the rotation of the E-plane pattern by 90° relative to the z-oriented EHD case, the directivity is not enhanced by the presence of the super-resonant Ag-based S-CNP and its maximum value remains around 1.5. Thus, as obtained for the passive S-CNP, the dipole resonance excited by an EHD located inside or outside a super-resonant, active, electrically small spherical S-CNP does not modify its directivity pattern. The varying NRR levels observed for the x-oriented EHD excitation of the Ag-based S-CNP in Figure 5 cannot be revealed through the directivity pattern alone. It requires the study of the associated near-field distributions, cf., the results in Section IV A.1.

B. Cylindrical CNPs

The results below represent a summary of our previous works [82] and [84]. The CC-CNP NRR values, directivity behaviours, and near- and far-field characteristics were studied thoroughly. In all of the cases discussed below, the MLS is driven by a constant current with $I_m = 1$ V. As noted in Section II, the MLS, as opposed to the ELS, is required to excite resonances in the plasmonic-based CC-CNPs. Unless otherwise stated, the MLS is located along the positive x-axis at a distance of $\rho_s = 12$ nm.

B.1 NRR and near-field distributions

In Figure 8 the NRR is shown as a function of the wavelength, λ_0, for (a) passive, ($\kappa = 0$) and (b) super-resonant Ag-, Au-, and Cu-based CC-CNPs.

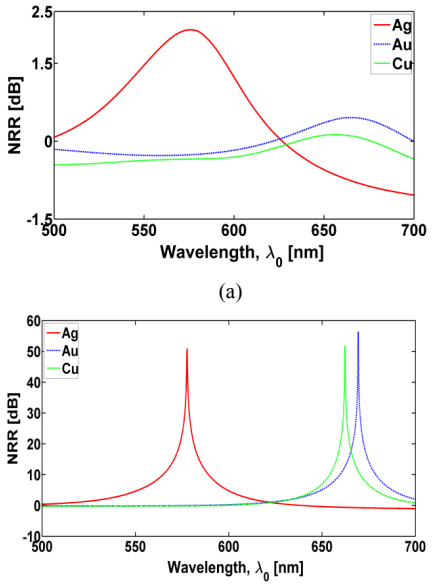

(a)

(b)

Fig. 8. The NRR as a function of the excitation wavelength, λ_0, for (a) passive and (b) active Ag-, Au-, and Cu-based CC-CNPs. In all cases, the MLS is located in their silica nano-cores at $\rho_s = 12$ nm, and $I_m = 1$V.

The super-resonances for the three CC-CNPs are achieved for $\kappa = -0.175$, $\kappa = -0.262$, and $\kappa = -0.309$, respectively. While the response of the passive CC-CNPs is found to be dominated by the large absorption losses, and thus low NRR values, the plasmonic material losses are vastly overcome when gain is included inside the silica nano-core. Thus, for the active CC-CNPs, significantly increased values of the NRR are obtained. The values of the NRR, the parameter κ and the wavelength λ_0 for the super-resonant Ag-, Au-, and Cu-based CC-CNPs are summarized in Table 2. As with the S-CNPs,

the Cu-based CC-CNP requires the largest magnitude of the parameter κ in order to excite its super-resonant dipole state. This outcome again arises because the losses are largest in the Cu-based CC-CNPs. It is interesting to contrast the results for the CC-CNPs summarized in Table 2 against those of the corresponding S-CNPs summarized in Table 1. For a given plasmonic material, the super resonances are attained at significantly larger wavelengths for the CC-CNPs than for the S-SNPs. Moreover, the super-resonant behaviour of the CC-CNPs requires significantly lower magnitudes of the gain parameter κ. Furthermore, while the absolute peak NRR values achieved for the CC-CNPs are lower than those of the S-CNPs, the relative increase of the NRR in active versus passive CNP cases is comparable (roughly around 50 dB) for both CNP geometries.

Parameter	Ag	Au	Cu
NRR [dB]	51.06	56.39	51.75
κ	-0.175	-0.262	-0.309
λ_0 [nm]	577.70	669.39	662.30

Tab. 2. Summary of various parameters for the super-resonant Ag-, Au-, and Cu-based CC-CNPs when the MLS is inside the nano-core at $\rho_s = 12$nm.

We next consider the CC-CNPs near-field behaviour in order to explain the NRR results reported in Figure 8. To this end, Figure 9 summarizes the near-field distributions of the magnetic field (or, more precisely, the quantity $20 \cdot \log_{10}|\boldsymbol{H}|$, where $\boldsymbol{H}$ is the total magnetic field normalized by 1 A/m) obtained for the MLS-excited Ag-based CC-CNP.

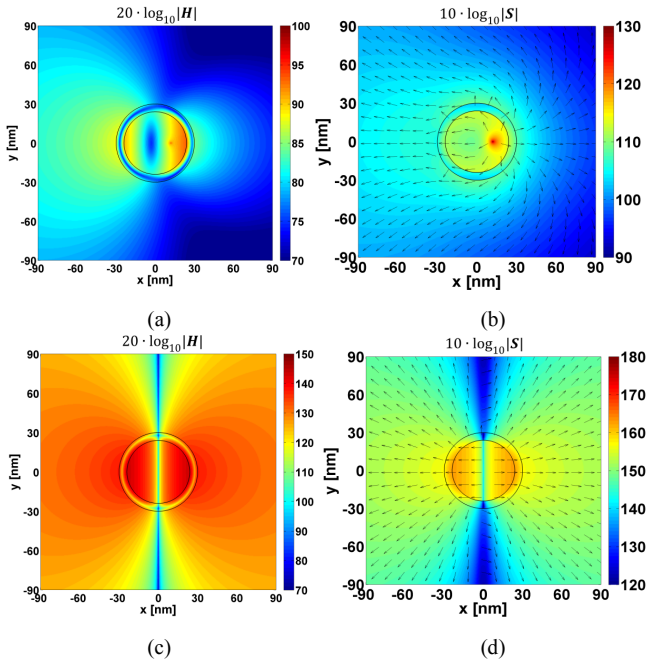

Fig. 9. The magnitude of the magnetic field of the (a) passive ($\kappa = 0, \lambda_0 = 575.69$ nm), and (c) super-resonant ($\kappa = -0.175, \lambda_0 = 577.70$ nm) Ag-based CC-CNP. The associated power flow densities (with the magnitude indicated by the colour and the direction indicated by the arrows) are shown in Figures 9(b) and 9(d), respectively. In all cases, the MLS is located along the x-axis inside the nano-core at $\rho_s = 12$nm. The cylindrical surfaces of the CC-CNP are included in the figure. Note that the dynamic ranges in Figures 9(c) and 9(d) are larger than those in Figures 9(a) and 9(b).

Figure 9(a) illustrates the passive Ag-based CNP ($\kappa = 0, \lambda_0 = 575.69$ nm) results; Figure 9(c) illustrates the super-resonant, active Ag-based CNP ($\kappa = -0.175, \lambda_0 = 577.70$ nm) results. The respective power flow densities (more precisely, the quantity $10 \cdot \log_{10}|\boldsymbol{S}|$, where $\boldsymbol{S}$ is the Poynting vector normalized by 1.0 W/m^2) are shown in Figures 9(b) and 9(d). The colours of the power density plots represent the magnitude of the Poynting vector, while the arrows show the direction of the power flow. The near-field and power flow distributions for the passive Ag-based CC-CNP, Figures 9(a) and 9(b), show a weak response which is a mixture of the monopole and dipole modes. The responses for the super-resonant case, Figures 9(c) and 9(d), are rather strong and of a clear dipolar shape. This confirms that the large values of the NRR reported in Figure 8(b) are indeed due to this excitation of a very strong and resonant dipole mode inside the CC-CNP. Although not shown here, the magnetic field and power flow distributions for the Au- and Cu-based CNPs in their super-resonant states resemble those of the Ag-based CNP shown in Figure 9.

As was the case with the S-CNPs, the super-resonances of the CC-CNPs are also in line with the (approximate) resonance condition [81, 98]

$$\frac{a}{b} \approx \sqrt[2n]{\frac{(\varepsilon_2' + \varepsilon_1')(\varepsilon_2' + \varepsilon_0)}{(\varepsilon_2' - \varepsilon_1')(\varepsilon_2' - \varepsilon_0)}}, n \geq 1 \qquad (4)$$

which holds for electrically small cases excited by the MLS (TE polarization) when the material losses are sufficiently small. When (4) is satisfied, the amplitude of the expansion coefficient of the scattered field in region 3 (exterior to the CNP) is maximized, thereby maximizing the radiated power and, hence, the NRR. As was the case for the S-CNPs, at least one of the parameters, ε_1' or ε_2', must be negative. This requirement is fulfilled here due to the positive values of ε_1' inside the active silica nano-core and the negative values of ε_2' associated with the plasmonic materials in the shells. For the Ag-based CC-CNP, with $\kappa = -0.175$, the super-resonant wavelength is 577.70 nm. At that wavelength we have $\varepsilon_1' = 2.02\ \varepsilon_0$, and $\varepsilon_2' = -14.49\ \varepsilon_0$. Inserting these values into (4), with $a = 24$ nm and $n = 1$ (since the super-resonance is due to the dipole mode), one obtains $b \approx 29.6$ nm. This is close to the exact value of 30 nm. The condition (4) is likewise satisfied for the Au-, and Cu-based CC-CNPs. The fulfilment of the approximate resonance condition (4) is further evidence that the plasmonic losses in the CC-CNPs have been vastly overcome upon inclusion the gain material inside their nano-cores. We note that for an ELS excitation (TM polarization), the corresponding resonance condition involves the permeabilities, rather than permittivities, of the CC-CNP. Since these are all positive in the CC-CNPs examined here, no resonances occur for this polarization.

As with the S-CNPs, the resonant behaviour of the three types of CC-CNPs is not restricted to having the MLS located in the interior of the nano-core. It also exists when the MLS is located inside their nano-shells and in their exteriors. This is

illustrated in Figure 10 which shows the NRR as a function of the MLS location, $\rho_s \in [0,50]$ nm, for the super-resonant Ag-, Au-, and Cu-based CNPs. As one can see, no enhancements of the NRR occur when the MLS is at and very close to the origin. This behaviour is due to the fact that the response is dominated by the monopole ($n = 0$) mode, which is non-resonant [81] for those locations. On the other hand, largest NRR values are obtained for MLS locations close to the inner surface of the plasmonic nano-shells. As expected from the S-CNP results, the response is found to decrease in magnitude as the MLS recedes away from the CC-CNP due to the decreased coupling between the two. Moreover, a dip in the NRR occurs for all cases as the MLS traverses the nano-shell region of the CC-CNPs. At the location of this local minimum, the response is still dominated by a dipole mode. Unlike the S-CNPs, the magnitude of the NRR for MLS locations in the exterior of the CC-CNPs, but close to its outer surface, is always below the maximum obtained near the interior surface of the nano-shell.

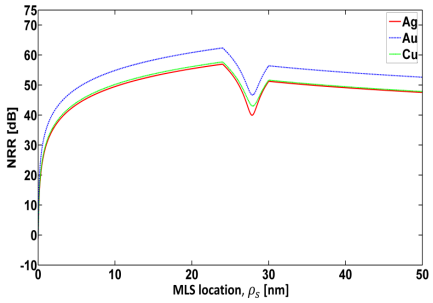

(b)

Fig. 10. The NRR as a function of the MLS location, $\rho_s \in [0,50]$ nm, for the super-resonant Ag-, Au-, and Cu-based CNPs.

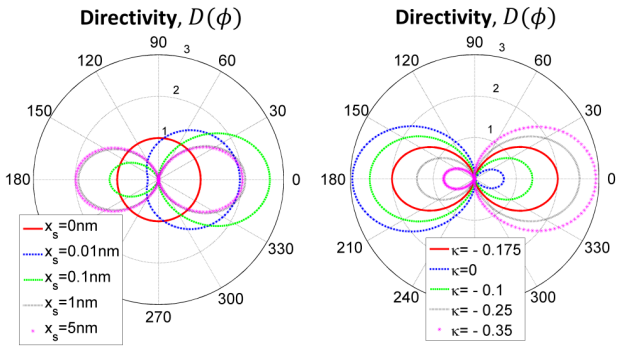

(a) (b)

Fig. 11. Directivities for the MLS-excited super-resonant Ag-based CC-CNP. The radius of the silica nano-core is 24 nm and the thickness of the silver nano-shell is 6 nm. In (a), the CC-CNP is super-resonant, and different MLS locations, x_s, inside the nano-core along the positive x-axis are considered. In (b), the MLS is located at x_s = 23 nm, near the inner surface of the nano-shell, and different values of the parameter κ are considered.

B.2 Directivity

With the large variation of the NRR as a function of the MLS location (cf., Figure 10), the associated varying strength of the excitation of the resonant modes of the CC-CNP, and its two dimensional nature, the directivity was assessed with expectations that there would be differences from the S-CNP behaviour as the MLS location is changed. To this end, Figure 11(a) shows the directivity for the super-resonant Ag-based CC-CNP ($\kappa = -0.175, \lambda_0 = 577.70$ nm) for the indicated MLS locations along the positive x-axis within the nano-core.

It is rather clear that large variations in the resulting patterns occur, particularly as the MLS is off-set from the origin at even a very small distance. For the super-resonant Ag-based CC-CNP, the directivity can be re-shaped from a perfectly monopolar pattern (attained at $\rho_s = x_s = 0$ nm) to a perfectly symmetric dipolar pattern (attained at $\rho_s = x_s = 5$ nm) simply by varying the MLS location. The former case agrees very well with the absence of any resonant phenomena observed in Figure 10 when the MLS is at or very near the center of the CC-CNP (NRR being around 0 dB). On the other hand, the latter case (NRR around 45 dB for $\rho_s = x_s = 5$ nm) indicates a strong excitation of the dipole mode, the latter being responsible for the large NRR values seen in Figure 10 as the MLS moves away from the centre of the CC-CNP. For the perfectly symmetric dipolar pattern in Figure 11(a), the maximum directivity of 2 is found along the $\phi = 0^o$ and $\phi = 180^o$ directions. However, larger values can be obtained for specific MLS locations (closer to the CC-CNP centre) for which the dominant response is a mixture of the monopole and dipole modes, rather than the resonant dipole mode alone. For instance, the result obtained for $\rho_s = x_s = 0.1$ nm illustrates this point; it is given in Figure 11(a).

We also note that the directivity of the active CC-CNPs can be re-shaped by slight adjustments of the parameter κ for a given MLS location. This is illustrated in Figure 11(b) where the directivities for the Ag-based CC-CNP are shown for $\lambda_0 = 577.70$ nm and the MLS located at $\rho_s = x_s = 23$ nm, near the inner surface of the nano-shell. For the examined values of κ that are larger than the super-resonant value ($\kappa = -0.175$), the main beam points in the $\phi = 180^o$ direction and approaches a maximum directivity of 3. In contrast, it points along the $\phi = 0^o$ direction for values of κ that are smaller than the super-resonant value.

Thus, the directivity of the spherical CNPs is unaffected by variations of its main design parameters, such as the EHD location and the value of the optical gain. On the other hand, the CC-CNP configurations exhibit directivity patterns which are highly influenced by even slight variations in the MLS location and the value of the optical gain constant.

V. Summary and Conclusions

The fundamental electromagnetic properties of several spherical and cylindrical, passive and active, coated nano-particles (CNPs) were reviewed. In particular, their potential for operation as nano-antennas, nano-amplifiers, and to some extent nano-sensors was emphasized. For both geometries, the CNPs consisted of a silica nano-core, layered concentrically with a nano-shell of silver, gold, or copper. In order to simulate an active CNP, gain was added to its nano-core region. The gain model, for simplicity, was taken to be a canonical, frequency independent model. The spherical CNPs were excited by an electric Hertzian dipole, whose orientation

was taken to be both tangential, as well as normal, to the spherical surfaces of the CNP. The cylindrical CNPs were excited by a magnetic line source. For both geometries, insights into the numerous effects of, e.g., the CNP material composition and the source locations and orientations were given on the basis of thorough numerical investigations of their total radiated powers, near-field and power flow distributions, and directivity properties.

It was shown that specific spherical, as well as cylindrical, active CNPs can be designed to be super-resonant and well-matched to their respective sources of excitation. As such, they are found to lead to very large enhancements of the total power radiated by the excitation sources, as compared to the total radiated power of the corresponding passive CNP designs. This super-resonant phenomenon was shown to be due to the excitation of a strong and resonant dipole mode in the examined CNPs. The large near-field and power flow density localization inside and just outside the examined CNPs indicate their potential as candidates for nano-amplifier and nano-antenna synthesis with enhanced radiation characteristics. For a given CNP material composition, these super resonances occur at much larger wavelengths for the cylindrical designs than for the spherical ones. Moreover, because of their infinite nature, the magnitude of the optical gain needed for the super-resonant behaviour is found to be lower in the cylindrical cases. Likewise, the absolute peak values of the total radiated power (as illustrated through the investigation of their NRR values) achieved for the cylindrical CNPs are lower than those for the spherical CNPs. Nevertheless, the relative increase of the NRR values in the active versus passive CNP cases is comparable (roughly around 50-55 dB) for both CNP geometries.

Some notable differences were elucidated for the two studied EHD orientations and the location of the EHD in the spherical CNP configurations. The strongest excitation of the resonant dipole mode and, thus, the largest attainable NRR values require the tangentially oriented EHD (with respect to the CNP surfaces) to be located inside the nano-core. The strongest responses for the normally oriented dipole occur if it is located just outside of the spherical CNPs. Because of the relative insensitivity of the super-resonance response to the EHD being located inside the CNP or in its exterior but immediately close to it, the spherical CNPs were identified as good candidates for a highly localized nano-sensor. In the cylindrical case, large NRR values were found for numerous line source locations, except for those when the source is at or very near the centre of the CNP. The response at those locations is dominated by the monopole mode, which cannot lead to any resonant phenomenon for the investigated CNPs.

The directivity of the EHD-excited CNPs was found to be unaffected by variations of its design parameters. This outcome included the dipole location and the value of the optical gain constant. Thus, a maximum directivity of 1.5 is obtained, basically the pattern of an isolated dipole. In contrast, the cylindrical CNP directivity patterns were found to be affected greatly by even a slight variation in the line source location or the amount of the optical gain. Directivity patterns ranging from perfect monopolar to perfect dipolar ones (with a maximum directivity of 2) to enhanced asymmetric patterns (with a maximum directivity of 3) can be achieved with small changes in the cylindrical CNP designs.

We conclude by noting that it was shown that the super-resonant, large NRR active CNP configurations are accompanied with extreme near-field and power flow density localizations, particularly when compared to their passive counterparts. The phenomena reviewed in this article demonstrate a large potential of using the proposed active CNPs as nano-antennas, nano-amplifiers, and/or nano-sensors. Although the present review focused on concentrically layered spherical and cylindrical designs, recent efforts have also considered the effects of layer eccentricity and non-canonical particle shapes [99-102] for the creation of directive near- and far-field beams. Future work will concentrate even more along the direction of studying various non-idealized passive and active CNP designs, in order to further highlight their profound benefits in a wide variety of optical applications.

REFERENCES

[1] C. Balanis, *Antenna Theory: Analysis and Design*, 2nd ed. New York: John Wiley & Sons, 1997.
[2] P. Bharadwaj, B. Deutsch and L. Novotny, "Optical antennas," *Adv. Opt. Photon*., vol. 1, pp. 438–483, Aug. 2009.
[3] M. Agio and A. Alù, Eds., *Optical Antennas*, Cambridge University Press, New York, 2013. Ch. 3: R. W. Ziolkowski, S. Arslanagić, and J. Geng, *Where high-frequency engineering advances optics. Active nanoparticles as nanoantennas*.
[4] A. Alù and N. Engheta, "Theory, modeling and features of optical nanoantennas," *IEEE Trans. Antennas Propag*., vol. 61, pp. 1508-1517, April, 2013.
[5] K. B. Crozier, A. Sundaramurthy, G. S. Kino and C. F. Quate, "Optical antennas: Resonators for local field enhancement," *J. Appl. Phys*., vol. 94, pp. 4632-4642, Oct. 2003.
[6] P. J. Schuck, D. P. Fromm, A. Sundaramurthy, G. S. Kino, and W. E. Moerner, "Improving the mismatch between light and nanoscale objects with gold bowtie nanoantennas," *Phys. Rev. Lett*., vol. 94, 017402, Jan. 2005.
[7] G. W. Bryant, F. J. García de Abajo and J. Aizpurua, "Mapping the plasmon resonances of metallic nanoantennas," *Nano Lett*., vol. 8, pp. 631–636, 2008.
[8] H. Guo, T. P. Meyrath, T. Zentgraf, N. Liu, L. Fu, H. Schweizer and H. Giessen, "Optical resonances of bowtie slot antennas and their geometry and material dependence," *Opt. Exp*., vol. 16, pp. 7756-7766, May 2008.
[9] H. Fischer and O. J. F. Martin, "Engineering the optical response of plasmonic nanoantennas," *Opt. Exp*., vol. 16, pp. 9144-9154, Jun. 2008.
[10] E. Hao and G. C. Schatz, "Electromagnetic fields around silver nanoparticles and dimers," *J. Chem. Phys*., vol. 120, pp. 357-366, Jan. 2004.
[11] I. Romero, J. Aizpurua, G. W. Bryant and F. J. García de Abajo, "Plasmons in nearly touching metallic nanoparticles: singular response in the limit of touching dimers," *Opt. Exp*., vol. 14, pp. 9988-9999, Oct. 2006.
[12] A. Alù and N. Engheta, "Hertzian plasmonic nanodimer as an efficient optical nanoantenna," *Phys. Rev. B*, vol. 78, 195111, Nov. 2008.
[13] A. Zhdanov, M. P. Kreuzer, S. Rao, A. Fedyanin, P. Ghenuche, R. Quidant and D. Petrov, "Detection of plasmon-enhanced luminescence fields from an optically manipulated pair of partially metal covered dielectric spheres," *Opt. Lett*., vol. 33, pp. 2749-2751, Dec. 2008.
[14] Jingjing Li, Alessandro Salandrino, and Nader Engheta , "Shaping light beams in the nanometer scale: A Yagi-Uda nanoantenna in the optical domain," *Phys. Rev. B*, vol. 76, 245403, Dec. 2007.
[15] T. H. Taminiau, F. D. Stefani and N. F. van Hulst, "Enhanced directional excitation and emission of single emitters by a nano-optical Yagi-Uda antenna," *Opt. Exp*., vol. 16, pp. 10858-10866, Jul. 2011.
[16] P. Ginzburg, A. Nevet, N. Berkovitch, A. Normatov, G. M. Lerman, A. Yanai, U. Levy and M. Orenstein, "Plasmonic resonance effects for

tandem receiving-transmitting nanoantennas," *Nano Lett*., vol. 11, pp. 220-224, Jan. 2011.
[17] Z. Liu, A. Boltasseva, R. H. Pedersen, R. Bakker, A. V. Kildishev, V. P. Drachev and V. M. Shalaev, "Plasmonic nanoantenna arrays for the visible," *Metamaterials*, vol. 2, pp. 45-51, 2008.
[18] J. Borneman, K.-P., Chen, A. Kildishev and V. Shalaev, "Simplified model for periodic nanoantennae: linear model and inverse design," *Opt. Exp*., vol. 17, pp. 11607-11617, Jul. 2009.
[19] A. Ahmadi and H. Mosallaei, "Plasmonic nanoloop array antenna," *Opt. Lett*., vol. 35, pp. 3706-2708, Nov. 2010.
[20] D. Dregely, R. Taubert, J. Dorfmüller, R. Vogelgesang, K. Kern and H. Giessen, "3D optical Yagi–Uda nanoantenna array," *Nat. Commun*., vol. 2, article 267, Apr. 2011.
[21] D. Wang, T. Yang and K. B. Crozier, "Optical antennas integrated with concentric ring gratings: electric field enhancement and directional radiation," *Opt. Exp*., vol. 19, pp. 2148-2157, Jan. 2011.
[22] J. Wen, S. Romanov, and U. Peschel, "Excitation of plasmonic gap waveguide by nanoantennas," *Opt. Exp*., vol. 16, pp. 9144-9154, Jun. 2008.
[23] A. Berrier, R. Ulbricht, M. Bonn, and J. G. Rivas, "Ultrafast active control of localized surface plasmon resonances in silicon bowtie antennas," *Opt. Exp*., vol. 18, pp. 23226-23235, Oct. 2010.
[24] P.-Y. Chen and A. Alù, "Optical nanoantenna arrays loaded with nonlinear materials," *Phys. Rev. B*, vol. 82, 235405, Dec. 2010.
[25] K. D. Ko, A. Kumar, K. H. Fung, R. Ambekar, G. L. Liu, N. X. Fang, and K. C. Toussaint, Jr., "Nonlinear optical response from arrays of Au bowtie nanoantennas," *Nano Lett*., vol. 11, pp. 61–65, Jan. 2011.
[26] N. Halas, "Plasmonics: an emerging field fostered by Nano Letters," *Nano Lett*., vol. 10, pp. 3816-3822, 2010.
[27] N. Engheta and R. W. Ziolkowski, Eds., *Metamaterials: Physics and Engineering Explorations*, Piscataway, NJ: IEEE Press, Wiley Publishing, 2006.
[28] W. Cai and V.M: Shalaev, *Optical Metamaterials*, Spring: Berlin, Germany, 2010.
[29] R. W. Ziolkowski, P. Jin and C.-C. Lin, "Metamaterial-inspired engineering of antennas," to *Proc. IEEE*, vol. 99, pp. 1720-1731, Oct. 2011.
[30] R. W. Ziolkowski and A. Kipple, "Application of double negative metamaterial to increase the power radiated by electrically small antennas," *IEEE Trans. Antennas Propag*., vol. 51, pp. 2626–2640, Oct. 2003.
[31] R. W. Ziolkowski and A. Erentok, "Metamaterial-based efficient electrically small antennas," *IEEE Trans. Antennas Propag*., vol. 54, pp. 2113–2130, Jul. 2006.
[32] A. Erentok and R. W. Ziolkowski, "Metamaterial-inspired efficient electrically-small antennas," *IEEE Trans. Antennas Propag*., vol. 56, pp. 691–707, Mar. 2008.
[33] R. W. Ziolkowski and A. Erentok, "At and beyond the Chu limit: passive and active broad bandwidth metamaterial-based efficient electrically small antennas," *IET Microwaves, Antennas & Propagation*, vol. 1, pp. 116-128, Feb. 2007.
[34] P. Jin and R. W. Ziolkowski, "Broadband, efficient, electrically small metamaterial-inspired antennas facilitated by active near-field resonant parasitic elements," *IEEE Trans. Antennas Propag*., vol. 58, pp. 318–327, Feb. 2010.
[35] L. J. Chu, "Physical limitations of omni-directional antennas," *J. Appl. Phys*., vol. 19, pp. 1163–1175, Dec. 1948.
[36] H. Thal, "New radiation Q limits for spherical wire antennas," *IEEE Trans. Antennas Propag*., vol. 54, pp. 2757-2763, Oct. 2006.
[37] S. Arslanagić, R. W. Ziolkowski, and O. Breinbjerg, "Radiation properties of an electric Hertzian dipole located near-by concentric metamaterial spheres," *Radio Sci*., vol. 42, RS6S16, doi:10.1029/2007RS003663, Nov. 2007.
[38] A. V. Zayats, I. I. Smolyaninov, and A. A. Maradudin, "Nano-optics of surface plasmon polaritons", *Phys. Rep*., vol. 408, pp. 131-314, Mar. 2005.
[39] R. W. Ziolkowski, "Ultra-thin metamaterial-based laser cavities," *J. Opt. Soc. Am. B*, vol. 23, pp. 451-460, Mar. 2006.
[40] J. A. Gordon and R. W. Ziolkowski, "The design and simulated performance of a coated nano-particle laser," *Opt. Exp*. 15, pp. 2622-2653, 2007.
[41] J. A. Gordon and R. W. Ziolkowski, "Investigating functionalized active coated nano-particles for use in nano-sensing applications," *Opt. Exp*., vol. 15, pp. 12562-12582, Oct. 2007.
[42] S. Arslanagić and R. W. Ziolkowski, "Active coated nano-particle excited by an arbitrarily located electric Hertzian dipole - resonance and transparency effects," *J. Opt. A*, vol. 12, 024014, Feb. 2010.
[43] M. T. Hill, "Status and prospects for metallic and plasmonic nano-lasers," *J. Opt. Soc. Am. B*, vol. 27, pp. B36-B44, Nov. 2010.
[44] I. E. Protsenko, A. V. Ushkoy, O. A. Zaimidoroga, V. N. Samoilov, and E. P. O'Reilly, "Dipole nanolaser," *Phys. Rev. A*, vol. 71, 063812 , Jun. 2005.
[45] A. K. Sarychev and G. Tartakovsky, "Magnetic plasmonic metamaterials in actively pumped host medium and plasmonic nanolaser," *Phys. Rev. B*, vol. 75, 085436, Feb. 2007.
[46] A. Mizrahi, V. Lomakin, B. A. Slutsky, M. P. Nezhad, L. Peng, and Y. Fainman, "Low threshold gain metal coated laser nanoresonators," *Opt. Lett*., vol. 33, pp. 1261-1263, Jun. 2008.
[47] A. Fratalocchi, C. Conti, G. Ruocco, "Three-dimensional ab initio investigation of light-matter interaction in Mie lasers," *Phys. Rev. A*, vol. 78, 013806, Jul.2008.
[48] C. Walther, G. Scalari, M. Ines Amanti, M. Beck, and J. Faist, "Microcavity laser oscillation in a circuit-based resonator," *Science*, vol. 327, pp. 1495-1497, Mar. 2010.
[49] X. F. Li and S. F. Yu, "Design of low-threshold compact Au-nanoparticle lasers," *Opt. Lett*., vol. 35, pp. 2535-2537, Aug. 2010.
[50] Q. Ding, A. Mizrahi, Y. Fainman and V. Lomakin, "Dielectric shielded nanoscale patch laser resonators," *Optics Letters*, Vol. 36, Issue 10, pp. 1812-1814, May 2011.
[51] A. K. Popov and V. M. Shalaev, "Compensating losses in negative-index metamaterials by optical parametric amplification," *Opt. Lett*. 31, pp. 2169-2171, Jul. 2006.
[52] J. A. Gordon and R. W. Ziolkowski, "CNP optical metamaterials," *Opt. Exp*., vol. 16, pp. 6692-6716, Apr. 2008.
[53] A. N. Lagarkov, V. N. Kisel, and A. K. Sarychev, "Loss and gain in metamaterials," *J. Opt. Soc. Am. B*, vol. 27, pp. 648-659, Apr. 2008.
[54] M. Wegener, J. L. García-Pomar, C. M. Soukoulis, N. Meinzer, M. Ruther and S. Linden, "Toy model for plasmonic metamaterial resonances coupled to two-level system gain," *Opt. Exp*., vol. 16, pp. 19785-19798, Nov. 2008.
[55] Z.-G. Dong, H. Liu, T. Li, Z.-H. Zhu, S.-M. Wang, J.-X. Cao, S.-N. Zhu and X. Zhang, "Resonance amplification of left-handed transmission at optical frequencies by stimulated emission of radiation in active metamaterials," *Opt. Exp*., vol. 16, pp. 20974-20980, Dec. 2008.
[56] K. Dolgaleva, R. W. Boyd, and P. W. Milonni, "The effects of local fields on laser gain for layered and Maxwell-Garnett composite materials," *J. Opt. A: Pure Appl*., vol. 11, 024002, Jan. 2009.
[57] A. Fang, Th. Koschny, M. Wegener, C. M. Soukolis, "Self-consistent calculation of metamaterials with gain," Phys. Rev. B, vol. 79, 241104(R), Jun. 2009.
[58] Y. Sivan, S. Xiao, U. K. Chettiar, A. V. Kildishev, and V. M. Shalaev, "Frequency-domain simulations of a negative-index material with embedded gain," *J. Opt. Soc. Am. B*, vol. 27, pp. 24060-24074, Dec. 2009.
[59] Y. Zeng, Q. Wu, and D. H. Werner, "Electrostatic theory for designing lossless negative permittivity metamaterials," *Opt. Lett*., vol. 35, pp. 1431-1433, May 2010.
[60] M. A. Noginov, G. Zhu, M. Bahoura, J. Adegoke, C. E. Small, B. A. Ritzo, V. P. Drachev and V. M. Shalaev, "Enhancement of surface plasmons in an Ag aggregate by optical gain in a dielectric medium," *Opt. Lett*., vol. 31, pp. 3022-3024, Oct. 2006.
[61] I. Avrutsky, "Surface plasmons at nanoscale relief gratings between a metal and a dielectric medium with optical gain," *Phys. Rev. B*, vol. 70, 155416, Oct. 2004.
[62] N. M. Lawandy, "Localized surface plasmon singularities in amplifying media," *Appl. Phys. Lett*., vol. 85, pp. 5040-5042, Nov. 2004.
[63] K. Okamoto, S. Vyawahare and A. Scherer, "Surface-plasmon enhanced bright emission from CdSe quantum-dot nanocrystals," *J. Opt. Soc. Am. B*, vol. 23, pp. 1674-1678, Aug. 2006.
[64] M. A. Noginov, "Compensation of surface plasmon loss by gain in dielectric medium," *J. Nanophoton*., vol. 2, 021855, Dec. 2008.
[65] K. F. MacDonald, Z. L. Sámson, M. I. Stockman, and N. I. Zheludev, "Ultrfast active plasmonics," *Nat. Photon*., vol. 3, pp. 55-58, Jan. 2009.
[66] M. A. Noginov, G. Zhu, R. Bakker, V. M. Shalaev, E. E. Narimanov, S. Stout, E. Herz, T. Suteewong, and U. Wiesner, "Demonstration of a spaser-based nanolaser", *Nature*, vol. 460, pp. 1110-1112, Aug. 2009.
[67] S. Xiao, V. P. Drachev, A. V. Kildishev, X. Ni, U. K. Chettiar, H. K. Yuan, and V. M. Shalaev, "Loss-free and active optical negative-index metamaterials", *Nature*, vol. 466, pp. 735-738, Aug. 2010.

[68] D. J. Bergman and M. I. Stockman, "Surface plasmon amplification by stimulated emission of radiation: quantum generation of coherent surface plasmons in nanosystems," *Phys. Rev. Lett*., vol. 90, 027402, Jan. 2003.
[69] M. I. Stockman, "Spasers explained," *Nat. Photon*., vol. 2, pp. 327-329, Jun. 2008.
[70] N. I. Zheludev, S. L. Prosyirnin, N. Papasimakis, and V. A. Fedotov, "Lasing spaser," *Nat. Photon*., vol. 2, pp. 351-354, Jun. 2008.
[71] M. I. Stockman, "The spaser as a nanoscale quantum generator and ultrafast amplifier," *J. Opt. A*, vol. 12, 024004, Jan. 2010.
[72] E. Plum, V. A. Fedotov, P. Kuo, D. P. Tsai, and N. I. Zheludev, "Towards the lasing spaser: controlling metamaterial optical response with semiconductor quantum dots," *Opt. Exp*., vol. 17, pp. 8548-8551, May 2009.
[73] A. I. Kuznetsov, A. E. Miroshnichenko, M. L. Brongersma, Y. S. Kivshar, and B. Luk'yanchuk, "Optically resonant dielectric nanostructures," *Science*, vol. 354, aag2471, Nov. 2016.
[74] S. Jahani and Z. Jacob, "All-dielectric metamaterials," *Nature Nanotech*., vol. 11, pp. 23-36, Jan. 2016.
[75] L. Zou, W. Withayachumnankul, C. M. Shah, A. Mitchell, M. Bhaskaran, S. Sriram and C. Fumeaux, "Dielectric resonator nanoantennas at visible frequencies," *Opt. Express*, vol. 21, pp. 1344-1352, 2013.
[76] P. Gutruf, C. Zou, W. Withayachumnankul, M. Bhaskaran, S. Sriram and C. Fumeaux, "Mechanically tunable dielectric resonator metasurfaces at visible frequencies," *ACS Nano*, vol. 10, pp. 133-141, 2016.
[77] S. Arslanagić, and R.W. Ziolkowski, "Influence of active nano particle size and material composition on multiple quantum emitter enhancements: their enhancement and jamming effects," *Progress in Electromagnetic Research,* vol. 149, pp. 85-99, 2014.
[78] S. Arslanagić, and R.W. Ziolkowski, "Nano-sensing of the orientation of fluorescing molecules with active coated nano-particles," *Fundamentals of Photonics and Nanostructures*, vol. 13, pp. 80-88, 2015.
[79] A. Erentok and R. W. Ziolkowski, "A hybrid optimization method to analyze metamaterial-based electrically small antennas," *IEEE Trans. Antennas Propagat*., vol. 55, pp. 731-741, Mar. 2007.
[80] A. Alù and N. Engheta, "Plasmonic and metamaterial cloaking: physical mechanisms and potentials," *J. Opt. A: Pure Appl. Opt*., vol. 10, 093002, Aug. 2008.
[81] S. Arslanagić, R.W. Ziolkowski and O. Breinbjerg, "Analytical and numerical investigation of the radiation and scattering from concentric metamaterial cylinders excited by an electric line source," *Radio Science*, vol. 42, doi: 10.1029/2007RS003644, Nov. 2007.
[82] S. Arslanagić, Y. Liu, R. Malureanu and R. W. Ziolkowski, "Impact of the excitation source and plasmonic material on cylindrical active coated nano-particles," *Sensors*, vol. 11, pp. 9109-9120, Sep. 2011.
[83] J. Geng, R. Jin, X. Liang and R. W. Ziolkowski, "Active cylindrical coated nano-particle antennas: polarization-dependent scattering properties," *J. Electromagnet. Wave Appl.* (JEMWA), DOI:10.1080/09205071.2013.809669, June 2013.
[84] S. Arslanagić, and R.W. Ziolkowski, "Directive properties of active coated nano-particles," *Advanced Electromagnetics,* vol. 1, no. 1, pp. 57-64, May 2012.
[85] E. M. Purcell, "Spontaneous emission probabilities at radio frequencies," *Phys. Rev.*, vol 69, 681, Jun. 1946.
[86] L. Novotny and B. Hecht, *Principles of Nano-Optics*, Cambridge University Press: New York, 2012.
[87] S. D. Campbell, and R. W. Ziolkowski, "The performance of active coated nanoparticles based on quantum dot gain media," *Adv. Optoelectron*., Vol. 2012, Article ID 368786, 2012.
[88] S. J. Oldenburg, G. D. Hale, J. B. Jackson, and N. Halas, "Light scattering from dipole and quadrupole nanoshell antennas," *Appl. Phys. Lett*., vol. 75, pp. 1063-1065, 1999.
[89] S. Kühn, U. Hakanson, L. Rogobete, and V. Sandoghadar, "Enhancement of single-molecule fluorescence using a gold nanoparticle as an optical nanoantennas," *Phys. Rev. Lett*., vol. 97, 017402, 2006.
[90] J-W. Liaw, C-L. Liu, W-M. Tu, C-S. Sun, and M-K. Kuo, "Average enhancement factor of molecules-doped coreshell (Ag@SiO2) on fluorescence," *Opt. Express*, vol. 18, pp. 12788-12797, 2010.
[91] B. S. Luk'yanchuk and V. Trenovsky, "Light scattering by a thin wire with a surface-plasmon resonance: bifurcations of the Poynting vector field," *Phys. Rev. B*, vol. 73, 235432, 2006.
[92] HY. She and L-W. Li, "Surface polaritons of small coated cylinders illuminated by normal incident TM and TE plane waves," *Opt. Express*, vol. 16, pp. 1007-1019, 2008.
[93] A. Alù and N. Engheta, "Enhanced directivity response from subwavelength infrared/optical nano-antennas loaded with plasmonic materials or metamaterials, "*IEEE Trans. Antennas Propag*., vol. 55, pp. 3027-3039, 2007.
[94] Z.Y. Li and Y. Xia, "Metal nanoparticles with gain toward single-molecule detection by surface-enhanced Raman scattering," *Nano Lett*., vol. 10, pp. 243-249, 2010.
[95] S. Y. Liu, J. Li, F. Zhou, L. Gan and Z-Y. Li, "Efficient surface plasmon amplification from gain-assisted gold nanorods," *Opt. Lett*., vol. 36, pp. 1296-1298, 2011.
[96] A. Alú and N. Engheta, "Polarizabilities and effective parameters for collections of spherical nano-particles of concentric double-negative (DNG), single-negative (SNG) and/or double-positive (DPS) metamaterial layers," *J. Appl. Phys.*, vol. 97, 094 310, May 2005.
[97] R. A. Shore, "Scattering of an electromagnetic linearly polarized plane wave by a multilayered sphere," *IEEE Ant. Propagat. Mag*., Vol. 57, pp. 69-116, Dec. 2015.
[98] A. Alú and N. Engheta, "Resonances in sub-wavelength cylindrical structures made of pairs of double-negative (DNG), and double-positive (DPS) or epsilon-negative (ENG) and mu-negative (MNG) coaxial shells," in *Proc. Intl. Conference on Electromagnetics in Advanced Applications*, Turin, Italy, Sept. 8-12, 2003.
[99] M. W. Knight and N. J. Halas, "Nanoshells to nanoeggs to nanocups: optical properties of reduced symmetry core-shell nanoparticles beyond the quasistatic limit," *New J. Phys*., vol. 10, 105006, 2008.
[100] R. Ø. Thorsen and S. Arslanagić, "Eccentrically-layered active coated nano-particles for directive near- and far-field radiation," *Photonics*, Vol. 2, pp. 773-794, 2015.
[101] S. D. Campbell and R. W. Ziolkowski, "Near-field directive beams from passive and active asymmetric optical nanoantennas," *IEEE J. Sel. Top. Quantum Electron*., Vol. 21, 4800112, 2014.
[102] A. E. Krasnok, C. R. Simovski, P. A. Belov, and Y. S. Kivshar, "Superdirective dielectric nanoantennas," *Nanoscale*, vol. 6, pp. 7354-7361, 2014.